Optimized split-flow deflector design for airflow drying systems using BP neural network coupled with NSGA-II algorithm

Xuehong Wu [a,b*], Dehua Yu [a], Yanyan Zhu [c], Yiming Xiao [a], Yong Liu [a], Shang Mao [a], Yanping Du [d,*]

a School of Energy and Power Engineering, Zhengzhou University of Light Industry, Zhengzhou, Henan 450000, China;

b International Joint Laboratory for Efficient Energy Conversion and Utilization of Henan Province, Zhengzhou, Henan 450000, China;

c Zhumadian Cigarette factory, China Tobacco Henan Industrial Co., Ltd., Zhumadian 463002, China

d School of Engineering, Lancaster University, Lancaster LA14YW, UK

** Corresponding author: wuxh1212@163.com, y.du17@lancaster.ac.uk*

Abstract: The non-uniform distribution of hot airflow and the high intensity of turbulence critically affect the effectiveness of airflow drying systems. In this study, numerical simulations were conducted to analyze the internal flow field characteristics of an airflow dryer. A novel split-flow deflector plate structure was designed and optimized using Response Surface Methodology (RSM) integrated with a backpropagation (BP) neural network and the NSGA-II algorithm. The results indicated that the designed split-flow deflector structure demonstrated superior performance compared with conventional arc-shaped designs. The optimized performance was achieved with a rotation speed of 190 r/min, deflector plate angle of 92°, and split-flow plate length of 380 mm. Compared to both the arc-shaped and pre-optimized configurations, the optimized split-flow deflector increased average airflow velocity by 4% and 39.2% and improved the airflow uniformity index by 11.8% and 14.5%, respectively. Furthermore, transient thermal analysis confirmed enhanced thermal stability as the outlet

temperature rapidly converges to the experimental benchmark (160°C), effectively mitigating thermal oscillations and intensifying gas-solid heat exchange. The findings provide both theoretical insight into the dynamic control of particle flows in dryers and a practical basis for the structural optimization of industrial airflow drying equipment.

Keywords: Airflow dryer; Structural optimization; Airflow uniformity; BP Neural network; NSGA-II

1. Introduction

Drying equipment is extensively applied across diverse sectors, including food processing[1], pharmaceuticals[2], chemical engineering[3], and agriculture[4]. These systems primarily utilize hot airflow to remove moisture efficiently, thereby enhancing both product quality and production efficiency. Depending on the underlying drying principles and specific application requirements, various configurations have been developed. Based on the heat source, common classifications include airflow drying[5], solar drying[6], and heat pump drying[7]. Among these, airflow drying is particularly favored due to its compact design, high heat transfer efficiency, rapid drying rate, and strong operational adaptability[8]. However, in practical applications, airflow dryers experience non-uniform distribution of hot air within the drying chamber. This uneven airflow leads to inconsistent heating and moisture removal across the material, causing variations in moisture content and localized agglomeration. Such issues detrimentally affect drying uniformity and ultimately compromise product quality consistency.

Improving airflow uniformity has become a major focus and persistent challenge in modern dryer research. Amjad et al. [9] conducted simulation studies on three distinct grain turner designs, revealing that a serrated structure significantly improved drying uniformity and dehydration efficiency. Chen et al. [8] designed and optimized an air distribution system for a microwave–infrared–hot air combined dryer. It was found that the drum-bed structure improved airflow

uniformity by 52.1%. Li et al. [10] investigated the effects of various airflow supply modes on sludge drying behavior and reported that a bottom-up flow combined with lateral auxiliary airflow substantially enhanced the drying efficiency and airflow uniformity. Ross et al. [11] focused on the spatial uniformity of the microwave field in a hybrid microwave-hot air dryer, effectively mitigating local overheating. Lan et al. [12] developed a CFD–DEM–IBM model to simulate gas–solid two-phase behavior in fluidized bed drying, demonstrating a high accuracy in predicting complex flow field uniformity. Recent studies indicated that conventional drying equipment frequently experienced uneven airflow distribution and material agglomeration. Nevertheless, these challenges can be effectively addressed through internal structural optimization and the integration of multi-field coupling designs, leading to improved flow uniformity and enhanced drying performance.

Introducing internal deflector plate structures has proven to be an effective strategy for improving the flow field uniformity in drying systems. Gai et al. [13] analyzed nine types of baffle configurations in a heat pump cabinet dryer, where the optimized design improved the airflow and the temperature uniformity by 52.7% and 85.3%, respectively, significantly enhancing the consistency and quality of fruit drying. Ahmad et al. [14] demonstrated that installing windbreak deflector plates in poultry house ventilation systems markedly enhanced the uniformity of both airflow and temperature distribution. Lv et al. [15] integrated V-shaped deflector plates into a microwave–hot air vibration dryer, reducing the air velocity variation from 1.1 m/s to 0.36 m/s and thereby substantially improving flow uniformity. Cao et al. [16] achieved improved airflow deflection and system uniformity by installing rectangular deflectors at the outlet of perforated air ducts and optimizing outlet angles. Wang et al. [17] enhanced airflow uniformity in drying chambers by adjusting deflector configurations in the air distribution chamber and adding deflector plates between material layers. Sabyasachi et al. [18], through CFD analyses, designed deflector screens with varying porosities; the optimal configuration improved airflow uniformity

by 64% in a fiber dryer, increasing the yield of high-quality fibers by 5%. Liu et al. [19] proposed a V-shaped perforated deflector that enhanced airflow uniformity by approximately 30% compared to conventional designs. Collectively, these studies highlighted the pivotal role of internal deflector structures in optimizing airflow distribution within drying systems.

The optimization of deflector structure parameters is inherently complex, often involving nonlinear, multi-objective problems. Artificial Neural Networks (ANNs) have gained widespread application in recent years due to their effectiveness in addressing structural optimization challenges across various engineering domains[20-22]. Notably, the Back Propagation (BP) neural network is particularly well-suited for establishing nonlinear mapping relationships between input design variables and output performance metrics[23]. For instance, Le et al. [24] combined a deep neural network with the artificial hummingbird algorithm to analyze the influence of material properties, thickness, and strain gradient parameters on the optimal design of functionally graded micro-scale structures. Zhang et al. [25] developed a surrogate strength model via a BP neural network to capture the nonlinear relationship between design parameters and structural response, subsequently integrating a genetic algorithm with reliability theory for multi-objective optimization. Similarly, Qi et al. [26] employed ANN-based optimization to refine the geometric parameters of a biomimetic shark skin riblet heat exchanger, achieving significant enhancements in airflow distribution and heat transfer performance.

The Genetic Algorithm (GA) was widely recognized for its effectiveness in optimizing the shape of deflector structures[27], while the improved Non-dominated sorting genetic algorithm II (NSGA-II) reduces computational complexity and achieves superior Pareto-optimal solutions[28]. The integration of the Back Propagation (BP) neural network with NSGA-II synergistically enhances model accuracy, minimizes trial-and-error costs, and accelerates the design process. This hybrid approach had been extensively applied to structural parameter optimization problems across diverse engineering fields[29-31]. For example, Liu et al. [32] employed the BP-

GA method to optimize L-shaped joints in composite sandwich structures, achieving a maximum relative error below 8% between predicted and experimental results, thereby substantially improving load-bearing capacity and stiffness. Jin et al. [33] developed a multi-objective optimization model based on an artificial neural network and utilized NSGA-II to optimize geometric parameters of an intercooler, resulting in a 20.2% enhancement in system energy efficiency. Subsequently, Jin et al. [34] incorporated a BP neural network surrogate within the NSGA-II framework for optimizing heat dissipation structures, yielding significant improvements in heat transfer performance. Fu et al. [35] applied NSGA-II to optimize multiple geometric parameters of a jet impingement cooling system, enhancing thermal performance while reducing pressure drop. Additionally, Xie et al. [36] compared the predictive capabilities of BP, GA-BP, and Support Vector Regression (SVR) models for evaluating the thermal performance of solar cavity receivers, demonstrating that the GA-BP model achieved the highest prediction accuracy. Collectively, these studies underscored the effectiveness of the BP-GA hybrid approach in addressing complex nonlinear, multi-objective parameter optimization challenges.

To summarize, uneven airflow distribution and thermal instability within drying equipment significantly impair drying quality, highlighting the necessity of deflector structure optimization for improving overall process stability and drying efficiency. This study investigates airflow dryers by proposing a novel split-flow deflector plate and analyzing its impact on internal flow characteristics and gas-solid heat exchange. Employing a D-optimal design of experiments, key structural parameters including the left deflector plate angle, split-flow plate size, and rotation speed were systematically varied, and corresponding performance metrics such as airflow uniformity index and average velocity were compared. Utilizing these datasets, a Back Propagation (BP) neural network coupled with the NSGA-II algorithm was developed to model the nonlinear relationships between structural parameters and performance indicators. Crucially,

transient thermal analysis was integrated to verify the improvements in thermal stability and temperature convergence of the optimized structure. The resulting optimization identified the deflector configuration that maximizes airflow uniformity and intensity, thereby providing an effective strategy to enhance the drying quality of materials.

2. Physical and Mathematical Models

2.1 Structural Design of the Airflow Dryer

The physical structure of the SH23A airflow dryer is presented in Figure 1, where Figure 1(b) specifically details the internal original arc-shaped deflectors. Based on these structural characteristics, three three-dimensional models were developed: a baseline model without any deflector structure, a model featuring the original arc-shaped deflector plates, and a model incorporating the proposed split-flow deflector structure, as illustrated in Figure 2. Figure 2(a) depicts the original dryer configuration, wherein arc-shaped deflector plates are evenly spaced within the drying chamber, while Figure 2(b) presents the optimized split-flow deflector design. In this arrangement, a distribution roller driven by a motor rotates to evenly disperse the material inside the chamber. Simultaneously, heated air enters through the inlet and is redirected upward to facilitate drying.

To clarify the specific airflow mechanism of the optimized design, the detailed working principle is illustrated in Figure 3. In this novel configuration, the inlet hot air is mechanically bifurcated by a horizontal split-flow plate. One portion of the airflow is guided through a series of small semi-circular deflectors to ensure uniform dispersion, while the remaining portion is directed by conventional angled deflectors. Crucially, the length of the split-flow plate serves as a vital governing parameter; it determines the volumetric distribution of hot air between the left and right regions, thereby directly influencing the overall flow field balance.

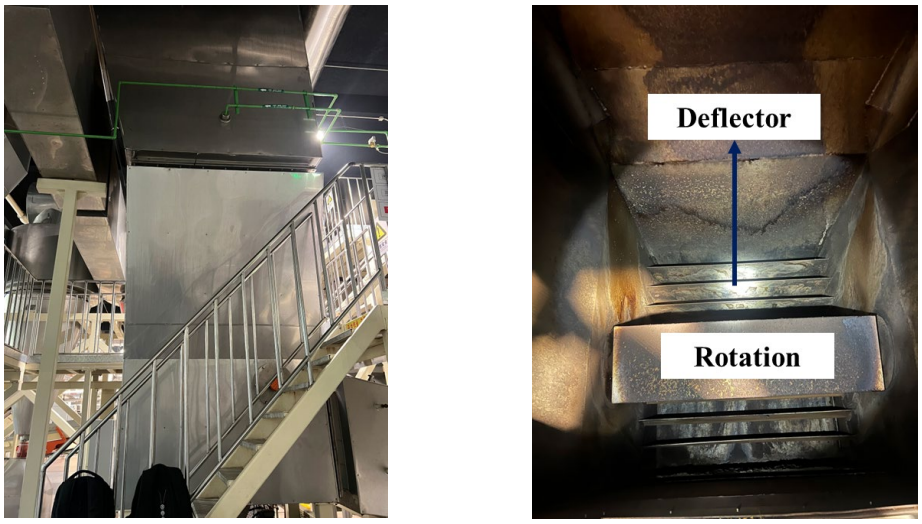

(a) photograph of the SH23A dryer (b) internal view of the original arc-shaped deflectors

148 Figure 1. Physical structure of the airflow dryer

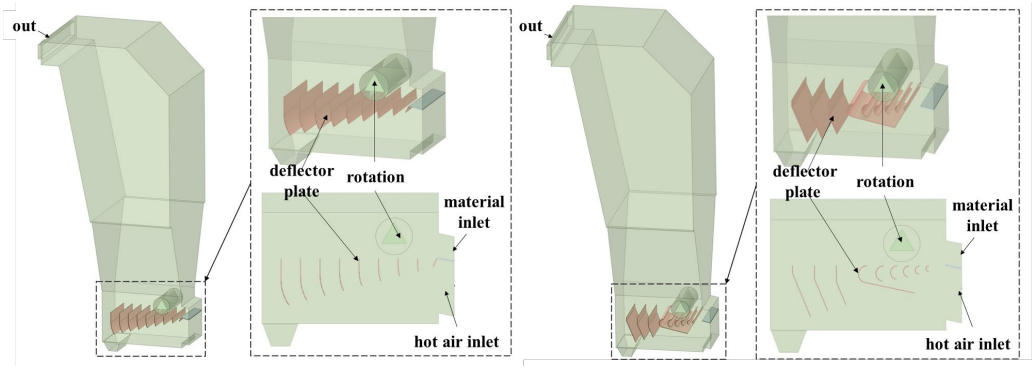

(a) Airflow dryer with original deflector structure (b) Airflow dryer with split-flow deflector structure

149 Figure 2. Three-dimensional models of the airflow dryer

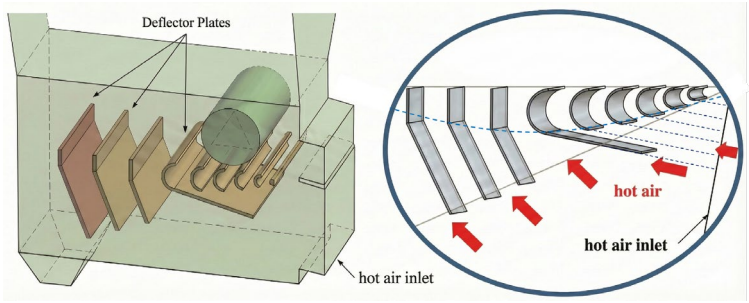

150

151 Figure 3. Schematic diagram illustrating the design principle of the split-flow deflector structure.

2.2 Mathematical Model and Boundary Conditions

2.2.1 Governing Equations

Given the high complexity of the drying process involving hot air and shredded tobacco within the airflow dryer, the following reasonable assumptions are made to simplify the analysis:

(1) The fluid is treated as an incompressible gas with constant density ρ. This simplification is adopted because the maximum airflow velocity corresponds to a mach number well below 0.3, and the relative density variation caused by the temperature drop (approx. 20°C) and species mixing during the stable operating phase is less than 5%, which is considered negligible for the flow field analysis;

(2) The drying process involves coupled heat and mass transfer. Therefore, the energy equation is incorporated to solve for the temperature field. The moisture content and temperature of the material change during the process, while the particle shape is assumed to remain constant to simplify the tracking;

(3) The ambient pressure is uniform and constant.

To characterize the internal flow behavior and thermal characteristics, and moisture transport within the dryer, the conservation equations for mass, momentum, energy, and species transport are employed. In the momentum equations, body forces are neglected, and only the viscous effects of air are considered. The incompressible Navier–Stokes (N–S) equations govern the flow analysis, while the energy conservation equation and species transport equation are introduced to solve for the temperature field and moisture distribution, respectively.

As hot air enters the drying chamber, it generates a complex flow field influenced by the deflector plates. Notably, significant turbulence, swirl, and flow separation occur near the deflector surfaces. To accurately resolve these complex flow characteristics, the Realizable k-ε

turbulence model is applied. Near-wall turbulence is modeled using standard wall functions. The continuity equation for incompressible flow is expressed as:

$$\frac{\partial \rho}{\partial t} + \nabla(\rho \mathbf{u}) = S_m \tag{1}$$

where S_m is the mass source term due to moisture evaporation from the particles.

Momentum Conservation Equation：

$$\rho\left(\frac{\partial \vec{u}}{\partial t} + \vec{\mathbf{u}} \cdot \nabla \vec{\mathbf{u}}\right) = -\nabla p + \mu \nabla^2 \mathbf{u} + \mathbf{F}_{pf} \tag{2}$$

The energy conservation equation is expressed as:

$$\frac{\partial(\rho h)}{\partial t} + \nabla(\rho \mathbf{u} h) = \nabla(\lambda \nabla T) + S_h \tag{1}$$

Turbulent kinetic energy equation：

$$\frac{\partial(\rho k)}{\partial t} + \nabla \cdot (\rho k \mathbf{u}) = \nabla \cdot \left[\left(\mu + \frac{\mu_t}{\sigma_k}\right)\nabla k\right] + G_k - \rho\varepsilon \tag{2}$$

Dissipation rate equation：

$$\frac{\partial(\rho\varepsilon)}{\partial t} + \nabla \cdot (\rho\varepsilon \mathbf{u}) = \nabla \cdot \left[\left(\mu + \frac{\mu_t}{\sigma_\varepsilon}\right)\nabla\varepsilon\right] + \rho C_1 S\varepsilon - \rho C_2 \frac{\varepsilon^2}{k + \sqrt{\nu\varepsilon}} \tag{3}$$

Species transport equation:

$$\frac{\partial(\rho Y_i)}{\partial t} + \nabla \cdot (\rho \mathbf{u} Y_i) = -\nabla \cdot \mathbf{J}_i + S_i \tag{4}$$

2.2.2 Governing Equations for the Discrete Phase

In the Lagrangian frame of reference, the motion and thermodynamic state of the tobacco particles are tracked individually. The trajectory of a discrete phase particle is predicted by integrating the force balance on the particle (Newton's second law).

Particle motion equation:

$$\frac{d\mathbf{u}_p}{dt} = F_D(\mathbf{u} - \mathbf{u}_p) + \frac{\mathbf{g}(\rho_p - \rho)}{\rho_p} + \mathbf{F}_{other} \tag{5}$$

where u_p is the particle velocity, u is the fluid velocity, and F_D is the drag force per unit particle mass.

Heat and mass transfer equations:

$$m_p c_p \frac{dT_p}{dt} = h_{conv} A_p (T_\infty - T_p) + \frac{dm_p}{dt} h_{fg} \tag{6}$$

where h_{conv} is the convective heat transfer coefficient, A_p is the particle surface area, h_{fg} is the latent heat of vaporization, and $\frac{dm_p}{dt}$ represents the rate of moisture evaporation.

2.2.3 Boundary Conditions

Air at atmospheric pressure enters the computational domain through the designated air inlet. The particulate phase, representing the material particles, is characterized by a density of 120 kg/m³ and a particle diameter of 2 mm. In the simulation, the initial velocity of the particles is assumed to be equal to that of the inlet gas phase. The detailed inlet boundary conditions are summarized in Table 1.

Air at atmospheric pressure enters the computational domain through the designated air inlet. The particulate phase, specifically representing shredded tobacco, is characterized by a density of 120 kg/m³ and a particle diameter of 2 mm, parameters selected based on actual factory production data. In the simulation, the initial velocity of the particles is assumed to be equal to that of the inlet gas phase. The inlet velocities are derived from the mass flow rates and the cross-sectional areas of the inlets. The detailed inlet boundary conditions, including temperature

and geometric parameters, are summarized in Table 1.

Table1. Inlet boundary conditions

Boundary	Temperature (℃)	Inlet Area (m^2)	Flow rate (kg/h)	Velocity (m/s)	Boundary type
Hot air inlet	180	0.5	51450	23.34	Velocity inlet
Material inlet	180	0.1814	1600	2.00	Velocity inlet

The gas-phase outlet boundary is modeled as a fully developed flow condition, with the outlet section extended both vertically and horizontally to ensure complete flow development. The outlet boundary is specified as a pressure outlet. For the particulate phase, the outlet boundary condition is defined as escape, permitting particles to exit the computational domain freely.

No-slip boundary conditions are imposed on all solid surfaces. For the dryer walls, deflector plate surfaces, and the bottom surface of the dryer, the discrete phase boundary condition is set to reflect, enabling particle rebound upon collision. Near-wall turbulence is addressed using an enhanced wall function approach. The turbulent viscosity ratio is a dimensionless quantity representing the ratio of turbulent to molecular viscosity (μ_t / μ), indicating the degree of turbulence development. The boundary conditions utilized in the simulation is detailed in Table 2.

Table 2. Boundary conditions and parameters

Boundary condition	Parameter	Boundary condition	Parameter
Turbulence intensity at material inlet (%)	2.90	Turbulence intensity at hot air inlet (%)	2.61
Turbulent viscosity ratio at material inlet	9.68	Turbulent viscosity ratio at hot air inlet	1968

2.3 Numerical Solution Approach

The airflow inside the dryer is modeled as an unsteady, viscous flow to capture the transient

behavior of the drying process accurately. To simulate this, a time-dependent solver is employed, which allows for the dynamic evolution of the flow field and interaction with the internal structures such as deflector plates. The governing Navier–Stokes equations, coupled with the energy conservation equation, species transport equation, and discrete phase model (DPM), are solved iteratively at each time step to account for the complex, time-varying flow phenomena. A two-way coupling scheme is adopted to account for the exchange of mass, momentum, and energy between the continuous airflow and the discrete tobacco particles.

Pressure–velocity coupling, a critical component in incompressible flow simulations, is handled using the SIMPLE algorithm. This algorithm efficiently resolves the coupling by iteratively correcting the pressure and velocity fields to satisfy the continuity equation, ensuring mass conservation throughout the domain. The transient approach is particularly important in this study because the interaction of hot airflow with the rotating distribution roller and deflector plates generates unsteady flow patterns that cannot be captured through steady-state simulations. This approach allows for a detailed investigation of turbulence fluctuations, flow separation, and recirculation zones that directly influence drying uniformity and efficiency.

In terms of numerical discretization, the spatial terms in the governing equations are discretized to ensure both accuracy and stability of the simulation. Diffusion terms, which represent viscous and conductive transport, are discretized using a second-order central difference scheme. This scheme provides a balanced and accurate approximation by considering the values at neighboring grid points symmetrically, minimizing numerical diffusion and preserving the physical fidelity of the gradients. For convection-dominated terms, such as those in the density momentum, energy, turbulence quantities, and species transport equations, a second-order upwind scheme is applied. The upwind discretization improves numerical stability by biasing the differencing in the direction of the flow, which helps to prevent non-physical oscillations and ensures robust convergence, especially in turbulent and high-velocity regions. To determine

the end of each iterative time step, a convergence criterion based on the residuals of the governing equations is imposed, with a threshold of 1×10^{-5} for all residuals. This ensures that the numerical errors are sufficiently minimized before advancing in time, leading to stable and reliable simulation results.

2.4 Grid Independence Verification

Prior to initiating the numerical simulations, it is crucial to verify that the mesh resolution does not significantly influence the accuracy of the results. While increasing the number of mesh cells generally enhances solution precision by better resolving flow features, it also substantially raises computational time and resource requirements. To achieve an optimal balance between accuracy and efficiency, a grid independence study was conducted.

Figures 4 and 5 illustrate the hexcore mesh topology employed for the airflow dryer, featuring a hybrid structure of hexahedral cores and tetrahedral transitions. To capture complex flow gradients, local refinement was applied in critical regions. Figure 4 details the grid distribution for the original arc-shaped deflector, while Figure 5 presents the optimized split-flow configuration. Specifically, Figure 5(b-e) highlights the generation of 12 prism inflation layers adjacent to both the deflector surfaces and the dryer inner wall. This structural arrangement ensures the precise resolution of near-wall velocity gradients and turbulent boundary layer effects, while meeting the requirements of standard wall functions.

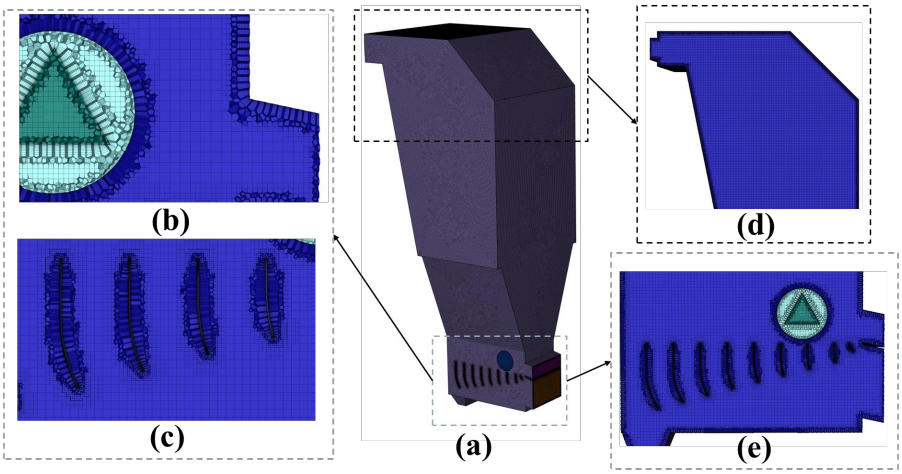

Figure 4. Hexcore mesh topology for the original arc-shaped deflector: (a) Global view; (b–e) Local refinement details

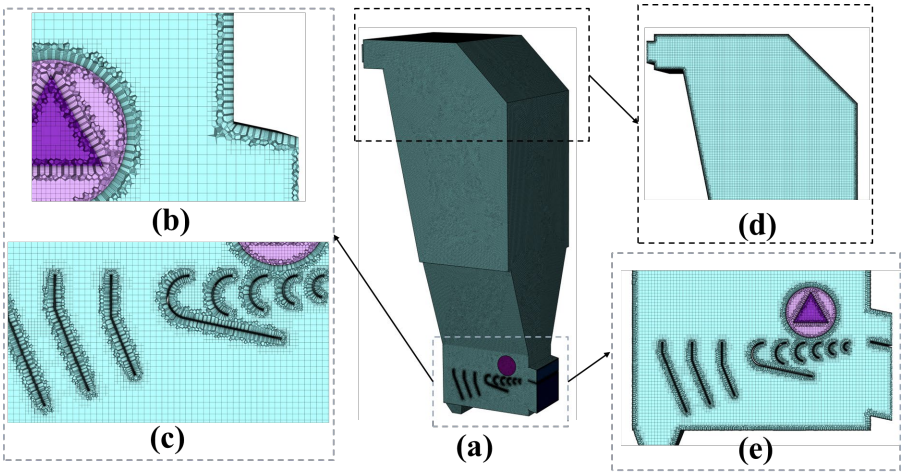

Figure 5. Detailed mesh for the optimized split-flow deflector: (a) Global view; (b–e) Prism inflation layers and near-wall refinement

For this verification, simulations are performed using the split-flow deflector plate configuration, and the uniformity index—an important metric reflecting the consistency of airflow distribution—is evaluated at three representative cross-sections located 1 meter (section a), 2.5 meters (section b), and 4.9 meters (section c) downstream from the distribution roller. The uniformity index at these sections is monitored while systematically increasing the total number of mesh cells. The results, summarized in Table 3, demonstrate the effect of mesh refinement on

predicted airflow uniformity.

As depicted in Figure 6, the relative difference in the uniformity index between the solutions with approximately 3.28 million and 8.52 million mesh cells is less than 5%, indicating that further mesh refinement yields only marginal improvements in accuracy. Based on these observations, a mesh size of about 3.28 million cells is chosen for all subsequent simulations. This choice ensures that the numerical results are reliable and sufficiently independent of mesh size while maintaining computational efficiency, thereby enabling detailed and cost-effective analysis of the airflow dynamics and optimization of the deflector plate design.

Furthermore, to ensure the applicability of the standard wall functions used in conjunction with the Realizable k-ε turbulence model, the non-dimensional wall distance y^+ was strictly monitored. For the selected mesh configuration (approx. 3.28 million cells), the first-layer grid height near the deflector surfaces was set to 0.5 mm. Post-processing inspection confirms that the average y^+ value on the deflector walls is maintained within the valid range of 30 to 300, with an area-weighted average of approximately 104 in high-velocity regions. This range perfectly satisfies the logarithmic law requirements of the standard wall function, ensuring accurate resolution of the turbulent boundary layer effects without demanding excessive computational resources.

Table 3. Results of grid independence verification

Mesh number	Uniformity index at a	Uniformity index at b	Uniformity index at c
786344	0.672	0.646	0.697
1515245	0.669	0.625	0.687
2292031	0.659	0.623	0.681
3285826	0.648	0.593	0.683
8523286	0.642	0.597	0.683

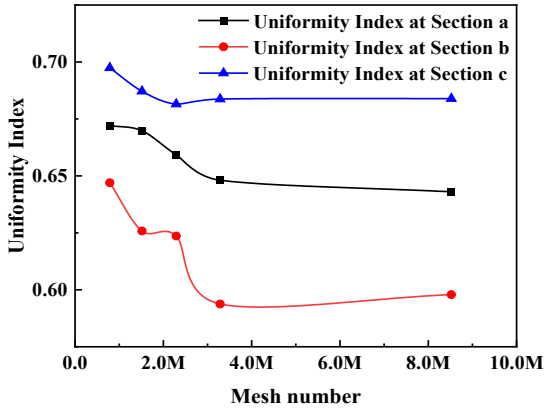

Figure 6. Grid independence verification

2.5 Evaluation of Flow Field Uniformity

To evaluate the uniformity of the airflow inside the dryer and quantitatively analyze the distribution characteristics of the deflector plate structure, relevant indicators related to airflow uniformity and flowability are introduced. The average velocity is calculated by the following formula:

$$\overline{|\mathbf{u}|}=\frac{\int_A|\mathbf{u}(x,y)|\,dA}{\int_A dA}\approx\frac{\sum_i|\mathbf{u}_i|\,A_i}{\sum_i A_i} \tag{7}$$

Where, $|\mathbf{u}(x,y)|=\sqrt{u^2+v^2+w^2}$ is the velocity magnitude at each point on the cross-section.

The uniformity index evaluation metric can comprehensively reflect the velocity distribution characteristics across the entire flow cross-section. It has the advantages of strong comparability and wide applicability. The expression for γ_v is：

$$\gamma_v=1-\frac{1}{2n}\sum_{j=1}^{n}\frac{\sqrt{\left(v_j-\overline{v}\right)^2}}{\overline{v}} \tag{8}$$

In the equation, the uniformity index γ_v ranges from 0 to 1. A higher value of γ_v indicates better flow uniformity. When γ_v =1, it represents an ideal uniform flow condition; when γ_v =0, it means the fluid passes through only one measurement point. Both of these are hypothetical conditions and do not occur in practical situations. Here, $\overline{v}$ denotes the average velocity over the cross-section, and v_j represents the velocity at each measurement point.

2.6 Multi-Objective Optimization Process of deflector Structure Parameters

The Backpropagation (BP) neural network is a topological multi-layer feedforward network trained using the error backpropagation algorithm. Compared with classic neural network frameworks, such as single-layer perceptrons which are limited to linearly separable problems, the BP model demonstrates superior advantages in non-linear mapping capabilities and self-adaptive learning. By utilizing gradient descent to minimize the error between predicted and actual outputs, the BP network can theoretically approximate any complex continuous function with arbitrary precision. This characteristic is particularly critical for this study, as the aerodynamic relationship between the deflector structural parameters and the internal flow field uniformity is inherently coupled, non-linear, and difficult to describe using explicit analytical equations.

In this study, a multi-layer BP neural network model featuring three hidden layers is developed to predict and optimize the performance of the airflow dryer based on key structural parameters of the deflector system. The neural network's input layer comprised the three critical design variables: the angle of the left-side deflector plate, the length of the split-flow plate, and the rotation speed of the distribution roller. These input parameters are essential because they directly influence the airflow patterns and drying efficiency within the chamber. The output layer of the network consists of two key performance indicators: the airflow uniformity index and the

average airflow velocity inside the drying chamber. These indicators are chosen because they effectively reflect the quality of the airflow distribution and the drying performance, respectively.

To determine the optimal number of neurons in the hidden layer, the Hecht–Nelson empirical method is applied as an initial theoretical reference. With n=3 input variables, the baseline recommendation is 7 neurons. However, considering the high complexity and strong nonlinearity of the turbulent flow field inside the dryer, a larger capacity is often required to ensure prediction accuracy. Therefore, based on the theoretical baseline and determined through extensive iterative trial-and-error testing, the number of neurons is increased to 11 for each of the three hidden layers. This specific configuration (3-11-11-11-2) is found to provide the optimal balance, effectively capturing high-dimensional nonlinear relationships while avoiding overfitting and excessive computational complexity. The detailed architecture of the BP neural network is graphically depicted in Figure 7.

To enhance the predictive accuracy and convergence speed of the BP neural network, a genetic algorithm (GA) is utilized to optimize the network's weights and biases. GA is a population-based stochastic optimization technique inspired by natural selection and evolutionary biology. This integration helps overcome the BP network's sensitivity to initial parameters and reduces the likelihood of becoming trapped in local minima during training. The entire optimization framework combining BP and GA is implemented using MATLAB. Further, to address the multi-objective nature of the deflector design problem, aiming to simultaneously maximize airflow uniformity and velocity, the Non-dominated sorting genetic algorithm II (NSGA-II) was employed.

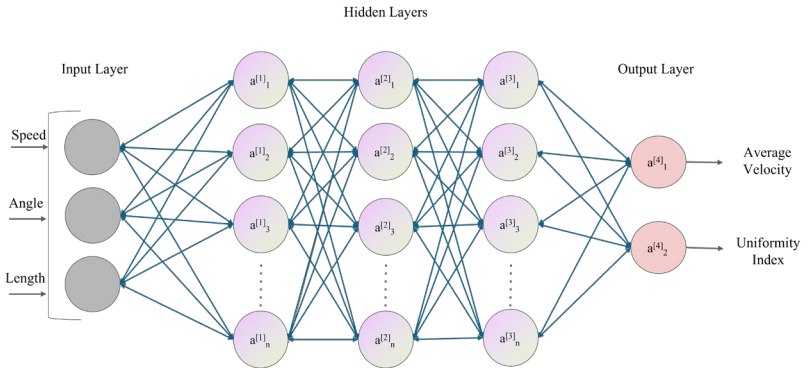

Figure 7. Structure diagram of BP neural network

A comprehensive flowchart of the combined BP–NSGA-II optimization process is presented in Figure 8, This flowchart outlines the sequential steps starting from population initialization, fitness evaluation via the BP model, non-dominated sorting, selection, crossover, mutation, and finally termination.

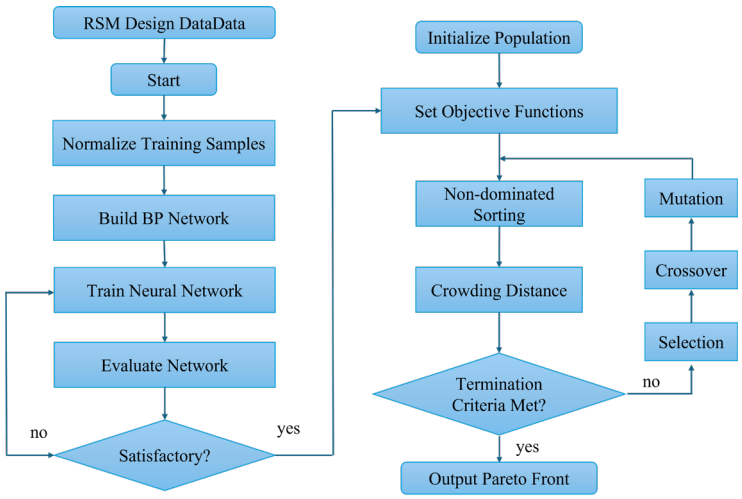

Figure 8. Flowchart of BP-GA structure

The hybrid approach effectively utilizes the predictive power of the neural network with the global search capability of NSGA-II, facilitating an efficient exploration of the design space and identification of optimal deflector structure parameters. This methodology offers a robust framework for enhancing dryer performance through intelligent structural optimization.

3. Results and Discussion

This chapter presents a comprehensive analysis of the airflow dryer's performance and structural optimization. The discussion is systematically organized into three main phases. First, the internal flow dynamics, thermal behavior, and particle drying characteristics are evaluated for different deflector configurations. Second, a multi-objective optimization framework combining RSM, BP neural network, and NSGA-II is implemented to determine the optimal structural parameters. Finally, the predicted optimal structures are rigorously validated through experimental comparison and detailed simulation analysis, confirming their superiority in enhancing airflow uniformity, particle dispersion.

3.1 Analysis of Flow Field Simulation Results

To evaluate the optimized split-flow design, comparative simulations are conducted against baseline structures. The analysis focuses on aerodynamic characteristics and turbulence intensity, thermal behavior, particle drying dynamics, and experimental validation, as detailed in the following subsections.

3.1.1 Velocity Field Characteristics under Different Deflector Structures

Figure 9 presents the velocity contours of the internal flow field within the airflow dryer under three different deflector configurations. As shown in Figure 9(a), after entering through the inlet, the material particles mix with the hot air, and the velocity distribution is relatively uniform before entering the main chamber. However, in the corner region, the mixed flow collides with the wall surface, causing the airflow to shift toward the left side of the chamber. This leads to a significant reduction in velocity in the central and right regions, forming a pronounced recirculation zone. As a result, the overall flow field becomes non-uniform, and the airflow uniformity is relatively poor. Figure 9(b) shows that after incorporating the arc-shaped deflector structure, the hot air is more evenly directed toward the upper region of the chamber by the

deflector plates. These improve the overall drying performance; however, local recirculation zones remain and are not entirely eliminated. In Figure 9(c), the introduction of the split-flow deflector structure further improves the hot airflow distribution. The size of the recirculation zones is noticeably reduced, the dispersion of material particles becomes more uniform, and agglomeration is effectively alleviated.

Using the split-flow deflector structure (parameters: n=230 r/min, θ=90°, d=400 mm), the average airflow velocity across five cross-sections on the XZ plane changed by +1.3%, +4.9%, –6.0%, –8.3%, and –0.4% compared with the original structure. Correspondingly, the airflow uniformity index increased by 12.6%, 12.7%, 3.8%, 4.0%, and 3.6%, respectively. These results indicate that the split-flow deflector structure provides notable improvements in enhancing airflow uniformity within the dryer.

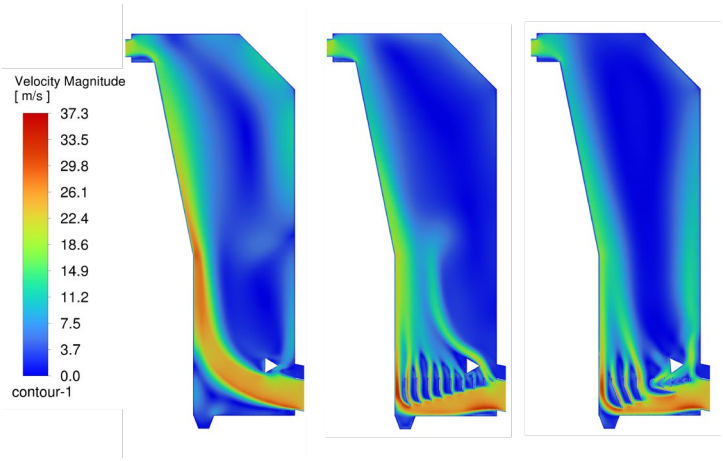

(a) No deflector plate (b) Arc-shaped deflector plate (c) Split-flow deflector plate

Figure 9. Airflow velocity contours under three different deflector structures

3.1.2 Comparative Analysis of Particle Spatial Distribution and Motion Behavior

Figures 10 and 11 illustrate the spatial distribution and motion trajectories of particles within the dryer under two different deflector structures. As shown in Figure 10, in the original structure,

particles are mainly concentrated on the right side of the dryer. After entering with the airflow, they rapidly settle and accumulate in the lower region of the chamber. Local recirculation zones and low-velocity stagnation areas are also observed, resulting in a relatively limited distribution range. In contrast, the split-flow deflector structure significantly improves particle flow behavior. The particle trajectories are more widely distributed within the drying chamber, with more dispersed motion in both vertical and horizontal directions. Recirculation is effectively mitigated, indicating that the structure enhances the spatial coverage of particle motion and promotes better contact with the hot air for drying.

Figure 11 further compares the particle distribution characteristics of the two structures in the XY plane. Under the original configuration, particles are mainly concentrated in the middle-lower region with relatively unidirectional flow. Localized stagnation zones with low velocities are evident. However, under the split-flow deflector structure, the particle trajectories cover the entire cross-sectional area more uniformly. Airflow directionality is improved, and the overall flow field becomes more homogeneous and coherent. This contributes to reducing particle deviation and avoiding problems such as localized over-drying or insufficient drying.

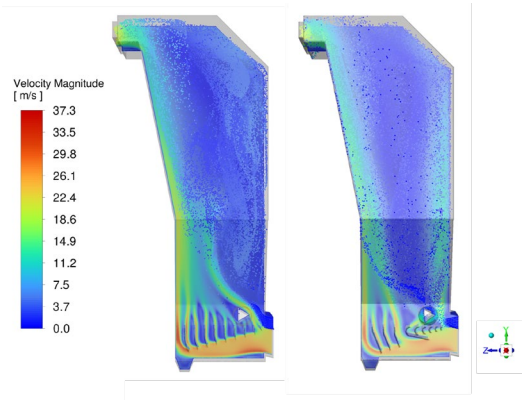

Figure 10. Particle distribution in the YZ plane for two airflow dryer structures

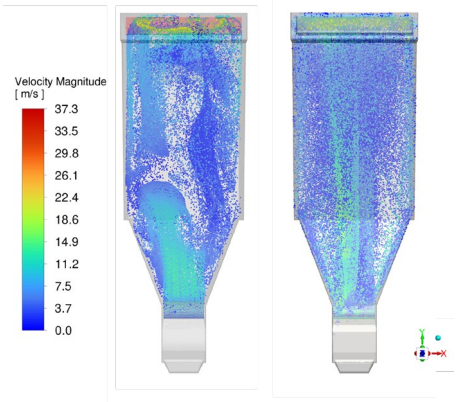

Figure 11. Particle distribution in the XY plane for two airflow dryer structures

Figures 12 and 13 compare the frequency distributions of particle residence time for the original and split-flow deflector configurations, respectively. As seen in Figure 12, the original structure shows a wide range of residence times, which reflects the presence of extensive turbulent zones and inefficient circulation regions. Consequently, particles experience prolong or irregular trajectories before exiting the chamber. Such conditions can lead to uneven drying with some particles being overexposed to hot air while others receive insufficient exposure. In contrast, Figure 13 demonstrates that the introduction of the split-flow deflector substantially narrows the residence time distribution. The majority of particles fall within the 1.0-2.5 s range, with markedly fewer particles experiencing extreme short or long residence durations. The corresponding frequency curve is smoother and more symmetrical, indicating a reduction in anomalous particle paths and a greater consistency in residence time. This behavior suggests that particle migration becomes shorter and more concentrated, thereby enhancing the stability and predictability of the drying process.

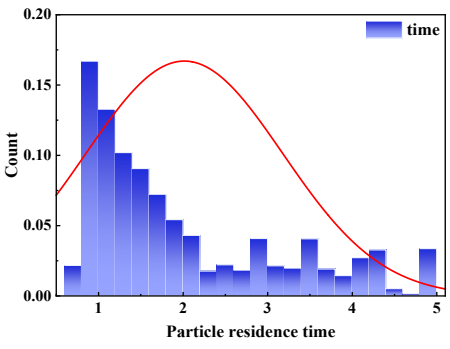

Figure 12. Residence time frequency distribution of particles in the original airflow dryer structure

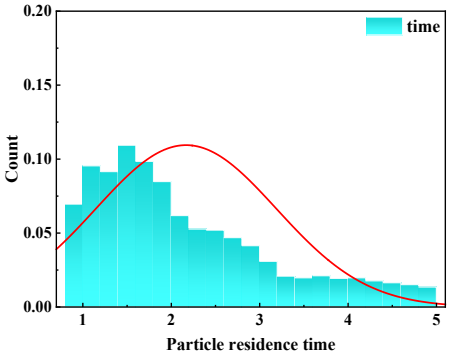

Figure 13. Residence time frequency distribution of particles in the split-flow airflow dryer structure

3.1.3 Evaluation of Turbulent Kinetic Energy Distribution and Flow Field Disturbance Characteristics

Figure 14 compares the distribution characteristics of turbulent kinetic energy (TKE) under three different deflector structures and evaluates their influence on flow field stability. In the structure without deflectors, the maximum TKE reaches 61.4 m^2/s^2. High-TKE regions are primarily concentrated near the wall surfaces, forming distinct energy dissipation zones that reduce overall flow stability. With the arc-shaped deflector structure, the maximum TKE increases to 75.57 m^2/s^2, while the area of high-TKE regions is the smallest among the three cases. This suggests that the arc-shaped structure can effectively concentrate turbulent energy, although local flow separation phenomena are still observed. The split-flow deflector configuration exhibits the highest maximum TKE, reaching 79.5 m^2/s^2. Owing to its multi-channel flow-splitting design, turbulent energy is more uniformly distributed throughout the chamber. This configuration maintains sufficient turbulence intensity to promote effective particle dispersion, while simultaneously improving the flow stability by preventing excessive localized energy concentrations.

The results indicate that the split-flow deflector structure increases the maximum TKE by 29.5% compared to the structure without deflectors, while simultaneously reducing the area of ineffective turbulence regions by 60%. Although the arc-shaped deflector effectively limits the spread of TKE, its overall turbulence intensity is lower than that of the split-flow structure, which may compromise drying performance. Therefore, the split-flow configuration enables more efficient use of turbulent energy, thereby contributing to improved drying efficiency.

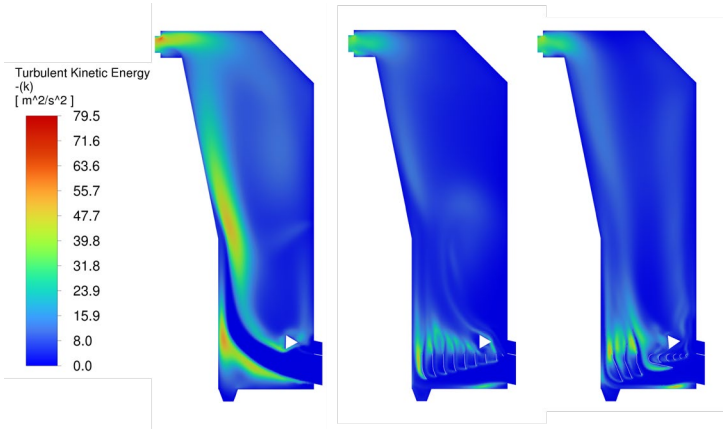

(a) No deflector plate (b) Arc-shaped deflector plate (c) Split-flow deflector plate

Figure 14. TKE contours under three different deflector structures

3.1.4 Analysis of Temperature Field and Drying Characteristics

The evaluation of thermal uniformity and particle motion figures 15 and 16 present a comparative analysis of particle temperature distributions in the YZ and XY planes, respectively. In the structure with the original arc-shaped deflector, the temperature field exhibits significant non-uniformity. As observed in the figures, the particle distribution is dominated by yellow regions, indicating that a large portion of the material remains at a medium temperature level and fails to reach the optimal heating state. Specifically, the airflow velocity in the left region of the chamber is relatively low. This insufficient aerodynamic force causes some particles to settle or move sluggishly, hindering effective heat exchange with the hot air. Furthermore, a distinct phenomenon is observed near the wall surfaces where particles tend to overheat due to prolonged contact time caused by local stagnation, which poses a potential risk to material quality.

In contrast, the optimized split-flow deflector structure significantly improves thermal performance. The particles throughout the chamber exhibit a uniform high-temperature distribution, primarily represented by red and orange colors. This indicates that the split-flow

design effectively eliminates the low-velocity zones and ensures that hot air fully penetrates the particle stream. Crucially, the improved flow aerodynamics significantly reduce the tendency of particles to adhere to the wall surfaces. This reduction in wall attachment minimizes the risk of localized overheating and material blockage, thereby ensuring both consistent heating and safer operation.

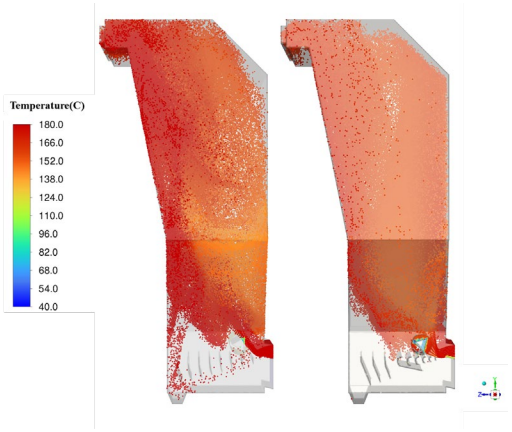

Figure 15. Comparative particle temperature profiles in the YZ plane

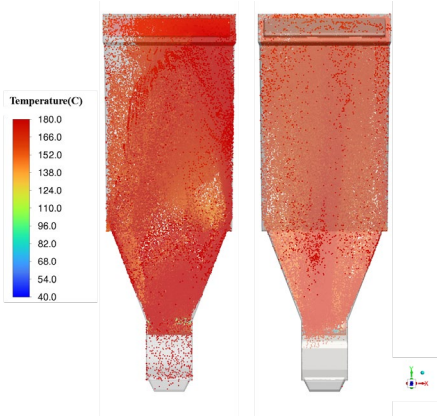

Figure 16. Comparative particle temperature profiles in the XY plane

Driven by the optimized thermal environment, the drying kinetics follow the gas-solid convective heat and mass transfer mechanism. Figures 17 and 18 illustrate the spatiotemporal evolution of particle moisture content on the YZ and XY planes from 2s to10 s. The color gradient quantitatively represents the progress of the mass transfer process, marking the transition from the initial high moisture content (red, mass fraction ~0.35) to the target range (yellow, ~0.13). At the initial stage (t=2s), particles entering the chamber exhibit high moisture characteristics. As they are transported upward under the guidance of the shunt guide vanes, intense heat and mass exchange occurs. By the 4s to 6s interval, particles achieve uniform dispersion across the XY and YZ planes with significantly attenuated moisture content, indicating that the drying process is approaching stability.

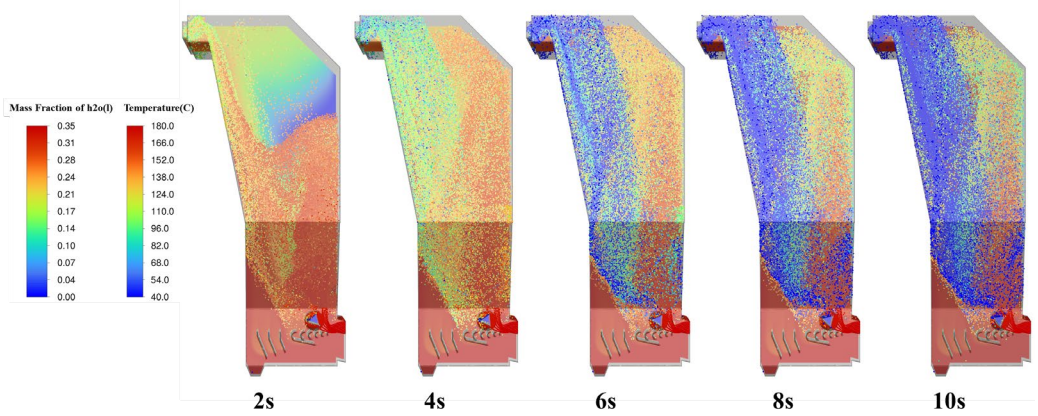

Figure17 Spatiotemporal moisture evolution in the YZ plane for the split-flow structure (2–10 s)

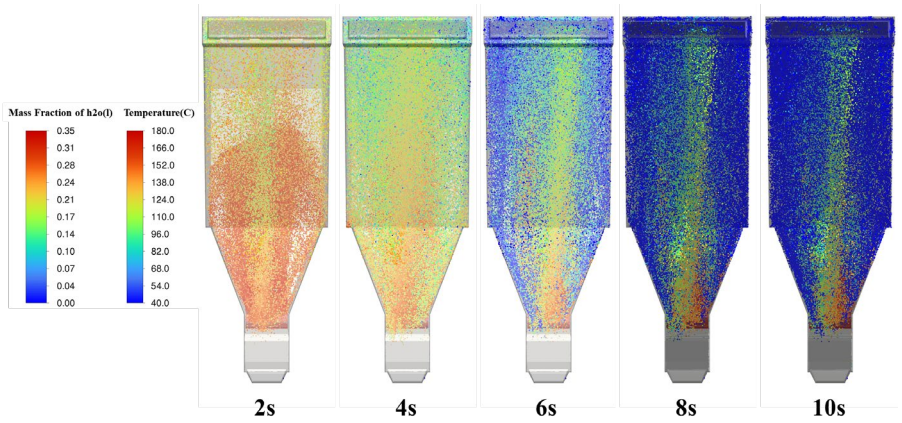

Figure 18. Spatiotemporal moisture evolution in the XY plane for the split-flow structure (2–10 s)

Figure 19 further reveals the microscopic characteristics of particle moisture distribution in the negative YZ direction during the steady-state drying stage (6s to 10s), elucidating the separation of drying states governed by fluid dynamics. In the central mainstream region, the particle distribution exhibits a uniform yellow characteristic. This indicates that the vast majority of the material has successfully reached the target moisture content of approximately 0.13, verifying the effectiveness of the shunt-type structure in ensuring the consistency of drying quality for the bulk material.

However, a distinct phenomenon is observed in the near-wall region, indicated by a persistent blue layer. This region represents particles with extremely low moisture content, signaling the

occurrence of over-drying. The physical mechanism underlying this phenomenon is primarily dominated by the boundary layer effect: due to fluid viscosity, a significant velocity gradient forms near the wall, causing particles entrapped in this region or adhering to the surface to experience velocity stagnation. Compared to particles in the mainstream, their significantly prolonged residence time leads to excessive moisture loss. Notably, in contrast to the more extensive stagnation zones in the original structure, the optimized shunt-type design effectively confines this over-dried region to a very narrow near-wall layer, thereby ensuring that the bulk tobacco material is maintained within the optimal drying range.

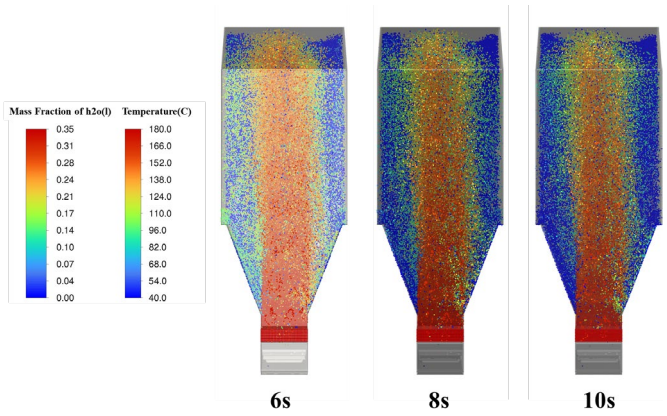

Figure 19. Particle moisture distribution in the YZ negative direction during the stable drying phase (6s–10s)

3.1.5 Experimental Validation of Heat and Mass Transfer Model

Figure 20 compares the transient outlet temperature evolution of both structures against the experimental benchmark (160°C). The close agreement between the simulated trends and experimental data validates the accuracy of the CFD-DEM model. Distinct dynamic behaviors are observed between the two designs. The arc-shaped structure (red line) exhibits pronounced thermal oscillation with large amplitudes, indicating significant flow instability. In contrast, the split-flow structure (blue line) demonstrates superior thermal stability. Although a minor temperature dip occurs during the initial phase, this is attributed to the intensified gas-solid heat

exchange, where rapid heat absorption by cold particles causes a temporary thermal lag. Subsequently, the profile converges rapidly with dampened fluctuations, confirming that the optimized design effectively mitigates unsteady disturbances.

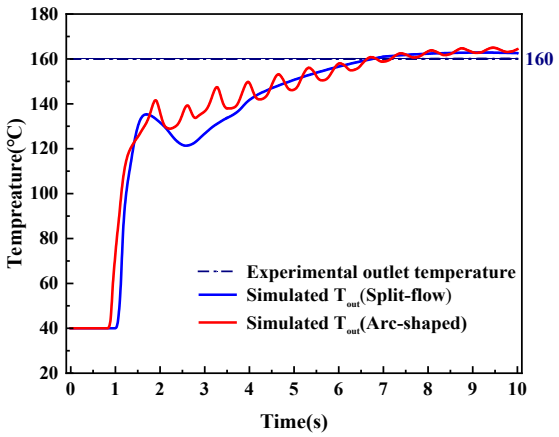

Figure 20. Comparison of simulated outlet temperatures against experimental data

3.2 Multi-Objective Optimization of deflector Structure Parameters

3.2.1 Response Surface Experimental Design

As shown in Figure 21, the simulation results for the airflow dryer with a split-flow deflector structure indicate that three structural parameters, including the rotation speed of the distribution roller (n), the inclination angle of the left deflector plate (θ), and the length of the split-flow plate (d) have significant influence on both airflow uniformity and intensity.

Based on a comprehensive analysis of the simulation results, the value ranges and specific settings for these parameters are determined. Detailed information is provided in Table 4.

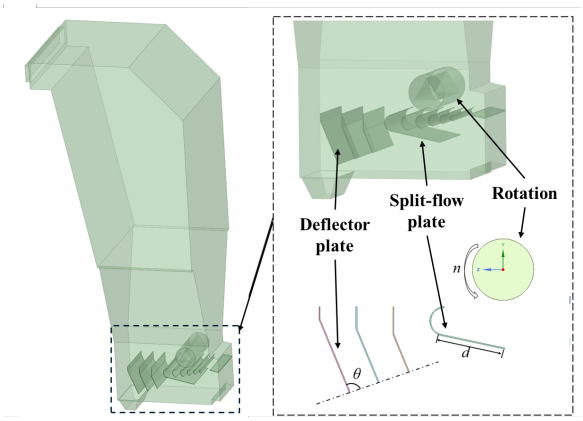

Figure 21. Airflow dryer with split-flow deflector structure

Table 4. Structural parameters of the deflector components

Parameter	Rotation speed n (r/min)	Deflector plate angle θ (°)	Split-flow plate length d (mm)
Values	60、150、180、210、230、277、325	80、90、100	350、400、450、500

The experimental design is a three-factor, multi-level scheme based on the response surface methodology (RSM), using the D-optimal design approach. The D-optimal method selects the most informative experimental points algorithmically, minimizing redundancy and reducing the number of simulations. Compared to random sampling or orthogonal design, it is better suited for nonlinear modeling problems.

The plane located 4.9 meters downstream from the distribution roller exhibits minimal velocity fluctuation and is therefore selected as the monitoring surface for evaluating airflow uniformity within the dryer. The simulated dataset generated using the D-optimal design is presented in Table 5.

Table 5. Simulated dataset based on D-optimal experimental design

No.	Speed n (r/min)	Angle θ (°)	Length d (mm)	Average velocity v (m/s)	Uniformity index
1	150	90	400	4.39	0.743
2	180	90	400	4.31	0.733
3	210	90	400	4.43	0.734
4	230	90	400	4.46	0.739
5	277	90	400	3.37	0.666
6	325	90	400	2.83	0.621
7	230	80	400	2.69	0.636
8	277	80	400	2.67	0.635
9	325	80	400	2.67	0.637
10	230	100	400	4.33	0.680
11	277	100	400	3.36	0.627
12	325	100	400	2.99	0.638
13	230	90	450	2.93	0.652
14	277	90	450	2.92	0.65
15	325	90	450	3.02	0.627
16	230	80	450	2.93	0.670
17	277	80	450	2.98	0.667
18	325	80	450	2.90	0.662
19	230	100	450	4.22	0.691
20	277	100	450	3.27	0.671
21	325	100	450	2.93	0.64
22	230	90	500	2.94	0.684
23	277	90	500	2.93	0.677
24	325	90	500	2.90	0.675
25	230	80	500	4.07	0.717
26	277	80	500	2.75	0.648
27	325	80	500	2.72	0.653
28	230	100	500	3.45	0.682
29	277	100	500	3.16	0.645
30	325	100	500	3.2	0.652
31	180	90	450	2.86	0.655
32	150	80	450	2.97	0.669
33	150	100	450	4.12	0.686
34	180	80	400	2.64	0.639
35	180	100	400	2.65	0.639

36	180	90	350	3.98	0.702
37	150	90	350	3.98	0.701
38	150	80	350	4.56	0.686
39	150	100	350	4.65	0.685
40	230	80	350	4.60	0.688
41	230	100	350	4.78	0.696
42	210	90	350	4.10	0.710
43	277	90	350	3.95	0.704

3.2.2 Validation of the Accuracy of the Neural Network Model

Firstly, the BP neural network is trained using the simulation data from Table 5. The network is designed with a three-layer architecture, including 3 input neurons, 4 neurons in the hidden layer, and 2 output neurons.

As shown in Figure 22, the coefficient of determination R^2 for the training set reachs 0.9990, while the R^2 for the testing set is 0.9978. The R^2 values for both datasets are very close (with a maximum difference of only 0.0012), indicating a uniform data distribution without significant outliers, which demonstrates successful model training and high prediction reliability.

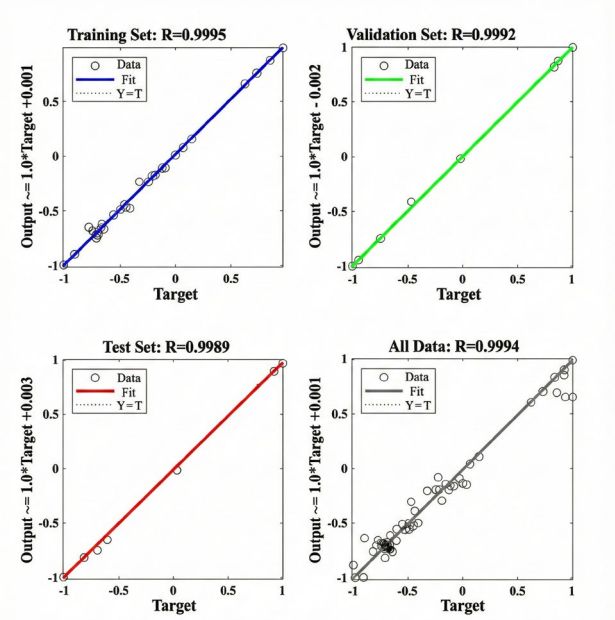

Figure 22. Linear regression plot of the neural network

Figures 23 and 24 compare the predicted and actual values of the two optimization indicators: uniformity index and average velocity. The prediction error for the uniformity index remains within 5%, while for the average velocity, the error is within 10%, verifying the accuracy of the model.

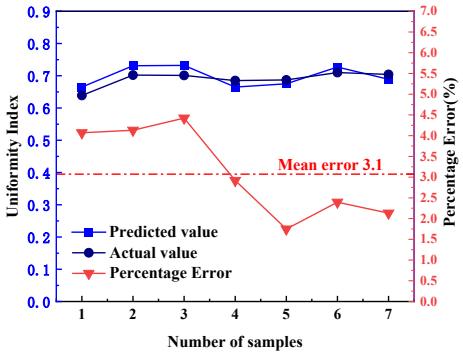

Figure 23. Predicted value vs. actual values of uniformity index by the neural network

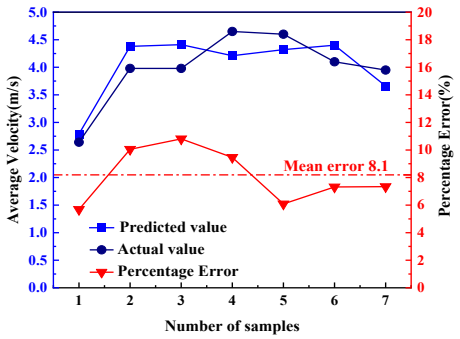

Figure 24. Predicted value vs. actual values of average velocity by the neural network

3.2.3 Optimization Results and Analysis of NSGA-II

The selected input factors are rotation speed (n), angle (θ), and length (d). The selected output parameters include the surface uniformity index and average velocity, as shown in Table 6.

Table 6. Range of influencing factors

Variable	Influencing factor	Lower limit	Upper limit
x_1	Speed n	150	325
x_2	Angle θ	300	390
x_3	Length d	30	60

The elite preservation coefficient is set to 0.4, with a population length of 50 and a maximum of 200 generations. The fitness function deviation threshold is defined as 1e-10. Based on these settings, multiple optimized solutions are obtained through computation, as shown in Figure 25.

The Pareto front is a widely used tool in multi-objective optimization problems, particularly effective for evaluating trade-offs between conflicting objectives. It represents a set of non-dominated solutions, in which no individual objective can be improved without degrading another under the given constraints. The final selection of an optimal solution depends on specific requirements, constraints, and practical application scenarios. Representative Pareto-optimal solutions are illustrated in Figure 25.

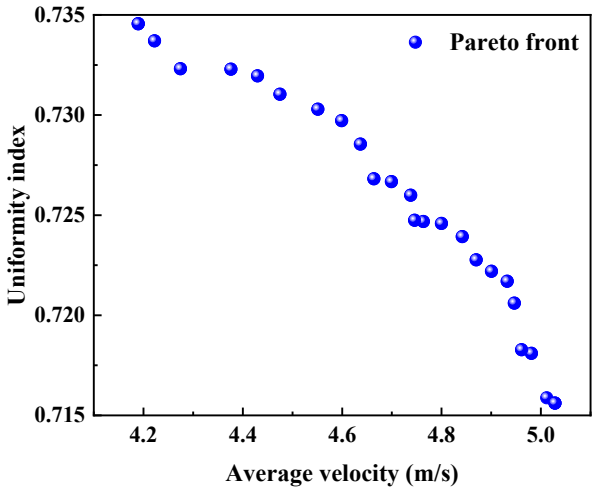

Figure 25. Pareto front of the multi-objective optimization results.

Several optimal reference solutions are selected from the optimization results, as listed in Table 7. The results indicate that adjusting the distribution roller speed, the inclination angle of the left-side deflector plate, and the length of the split-flow plate can significantly improve both the airflow uniformity and the average velocity inside the airflow dryer. These improvements demonstrate that appropriate modifications to the three structural parameters lead to a more uniform internal flow field and enhanced flow capacity, thereby improving both the quality and efficiency of material drying.

Under identical hot air and material inlet conditions, compared with the original configuration (parameters: n=230 r/min, θ=80°, d=400 mm), the airflow uniformity index predicted values of

the three optimized structures improve by 12.7%, 12.6%, and 12.3%, respectively, and increases in average airflow velocity by 41.3%, 41.7%, and 42.6%.

Table 7. Selected optimal reference points from the optimization results

Reference structure	Speed n (r/min)	Angle θ (°)	Length d (mm)	Average velocity v (m/s)	Uniformity index
Predicted structure (1)	180	92	380	4.59	0.729
Predicted structure (2)	190	92	380	4.62	0.728
Predicted structure (3)	190	92	370	4.69	0.726

3.3 Validation of Predicted Results

Figure 26 presents the airflow velocity contours for three predicted deflector structures. The results indicate that the constructed split-flow deflector configurations effectively guide hot airflow, resulting in a more uniform velocity distribution within the drying chamber. This leads to a more consistent drying environment for the dispersed material.

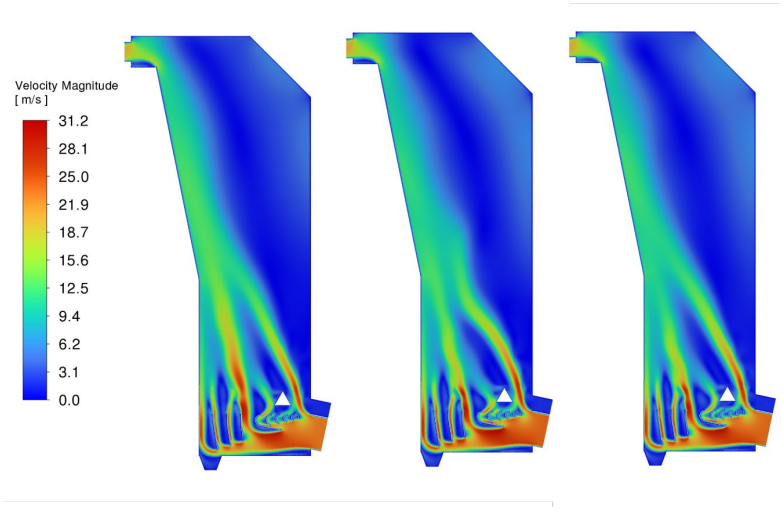

(a) Prediction structure (1) (b) Prediction structure (2) (c) Prediction structure (3)

Figure 26. Velocity contour plots of airflow for the three predicted deflector plate structures

Figure 27 further analyzes the error between simulation predictions and experimental

measurements for the three configurations. The structure optimized using the BP-GA algorithm shows high predictive accuracy, with an average velocity error of 7% and a uniformity index error of only 2%. Compared to the original arc-shaped deflector plate structure, the three predicted structures show respective improvements in average airflow velocity of 0.9%, 4.0%, and 2.3%, and increases in uniformity index of 9.9%, 11.8%, and 11.5%. When compared with the pre-optimized split-flow structure (n=230 r/min, θ=80°, d=400 mm), the improvements in average velocity are 36.7%, 39.2%, and 38.2%, while the uniformity index increases by 12.6%, 14.5%, and 14.2%, respectively. Among them, prediction structure (2) demonstrates the best performance across both key indicators.

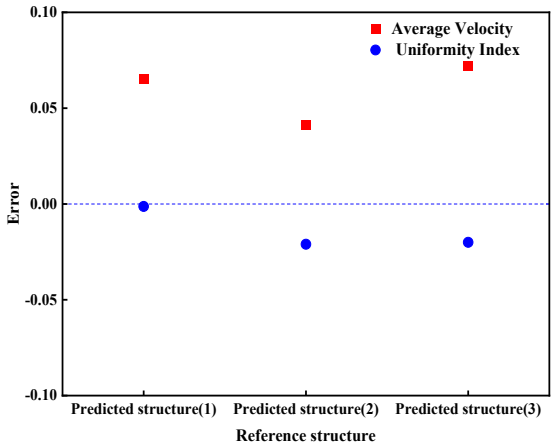

Figure 27. Comparison of prediction and actual values for the three predicted structures

Figure 28 compares the particle spatial distribution and motion trajectories between the pre-optimized split-flow deflector structure (parameters: n=230 r/min, θ=90°, d=400 mm) and prediction structure (2). Although the split-flow structure already alleviates particle sedimentation and limited spatial coverage issues compared to the arc-shaped design, some localized aggregation and path deviation due to rotation-induced disturbances remain. In contrast, prediction structure (2) significantly expands the particle dispersion range within the chamber. The particle trajectories are more spatially divergent and uniform, the disturbance

effect from the rotation component is noticeably reduced, and problems such as stagnation and accumulation in the lower region are effectively mitigated.

Figure 29 provides a cross-sectional comparison of particle distribution in the XY plane. The optimized structure notably enhances particle coverage and distribution uniformity across the section, with improved coordination between particle movement and airflow.

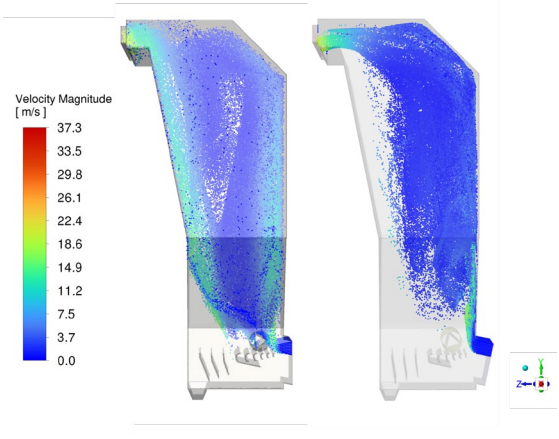

Figure 28. Comparison of particle distribution in the YZ direction between the original and predicted structure (2)

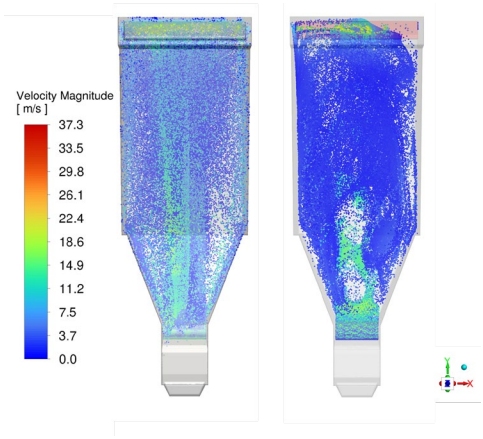

Figure 29. Comparison of particle distribution in the XY direction between the original and predicted structure (2)

Figure 30 shows the residence time frequency distribution of particles under prediction structure (2). Compared with the pre-optimized design (as shown in Figure 13), prediction structure (2) exhibits a slightly broader residence time range, primarily concentrated between 2–4.5s. However, the frequency curve is smoother with smaller fluctuations. In contrast, the pre-optimized structure presents a sharp frequency peak between 1–2.5s with more irregular fluctuations, indicating greater dispersion in particle trajectories. The results from prediction structure (2) suggest that internal flow disturbances are significantly reduced, particle paths are more coherent, and the average residence time is extended. This contributes to a more uniform spatial distribution and improved drying time efficiency, reducing the risk of localized under-

drying or over-drying and highlighting its superiority in particle drying quality control.

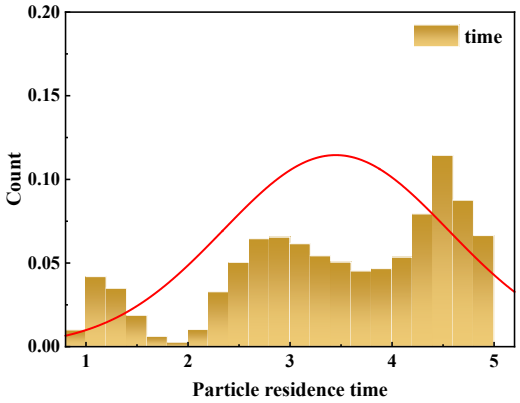

Figure 30. Residence time frequency distribution of particles inside the airflow dryer with the predicted structure (2)

Figure 31 illustrates the temporal variation of the airflow uniformity index across five cross-sections (A: 1 m from the roller center; B: 2 m; C: 3.5 m; D: 4.9 m; E: outlet plane) in the XZ plane of the airflow-based tobacco dryer. Analysis indicates that in region A, which is closest to the roller, all three optimized Deflector plate structures outperform the unoptimized split-flow design. These optimized structures are more effective in directing hot air and mitigating disturbances caused by the roller's rotation, thereby ensuring a more uniform drying effect for newly entering tobacco particles.

As the cross-sectional plane moves from A to D, the uniformity index exhibits a more stable variation trend. The optimized split-flow Deflector structures demonstrate significantly better performance in terms of hot air distribution uniformity compared to both the unoptimized split-flow and the original arc-shaped designs. At the outlet plane E, although the uniformity indices of different structures eventually converge with minor differences, the optimized structures maintain superior overall stability throughout the drying process. This enhanced stability provides critical assurance for the consistency and quality of tobacco drying.

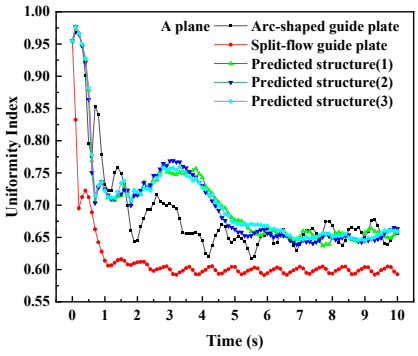

(a) Variation of uniformity index for five structures on plane A

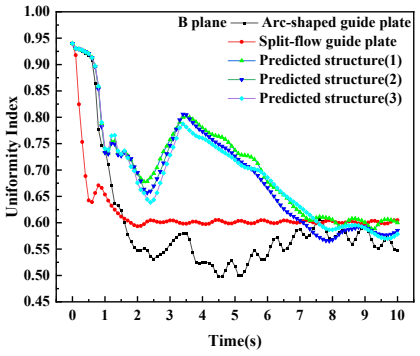

(b) Variation of uniformity index for five structures on plane B

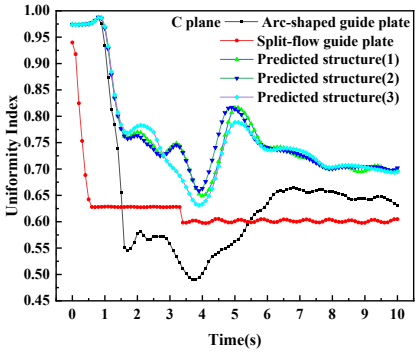

(c) Variation of uniformity index for five structures on plane C

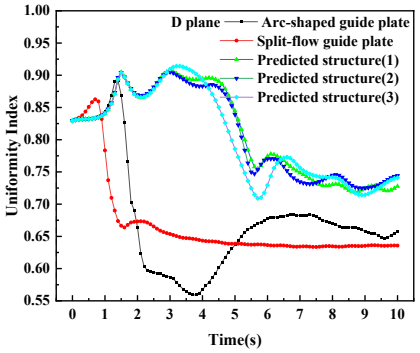

(d) Variation of uniformity index for five structures on plane D

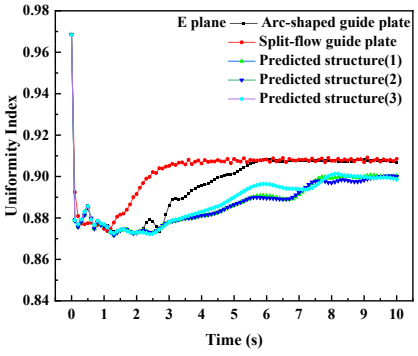

(e) Variation of uniformity index for five structures on plane E

Figure 31. Variation of uniformity index on different planes for the five structures

4. Concluding Remarks

This study proposed and evaluated a novel split-flow deflector plate configuration for airflow dryers. By integrating flow field analysis with multi-objective optimization, the following key conclusions were drawn:

(1) Hydrodynamic performance enhancement: Comparative analysis revealed that the inadequate flow guidance in the conventional arc-shaped deflector plate leads to pronounced velocity non-uniformities. In contrast, the optimized split-flow deflector plate enables more efficient utilization of turbulent energy. Compared with the original arc-shaped deflector plate, the optimized design improved the average airflow velocity by 4.0% and increased the uniformity index by 11.8%. This improvement translates into more consistent particle trajectories and reduced agglomeration.

(2) Thermodynamic stability and drying quality: The optimized structure demonstrates superior performance in coupled heat and mass transfer. Unlike the pronounced thermal oscillations observed in the arc-shaped deflector plate, the split-flow deflector plate exhibits excellent thermal stability, with the outlet temperature rapidly converging to the experimental benchmark (160℃). The initial thermal lag confirms the intensified gas-solid heat exchange facilitated by the optimized design. Furthermore, spatiotemporal analysis indicates that this structure effectively mitigates the over-drying phenomenon induced by the boundary layer effect. By confining the low-velocity stagnation zone to a narrow near-wall layer, the design prevents excessive moisture loss and ensures uniform drying quality for the bulk material.

(3) Optimization strategy and parameters: The coupling of BP-NSGA-II with flow field analysis proved to be an effective strategy for identifying parameter combinations that balance turbulence intensity with flow uniformity. The resulting prediction model achieved high accuracy (error < 5% for the uniformity index). The optimal performance was achieved with a rotation speed n of

190 r/min, Deflector plate angle θ of 92°, and Split-flow plate length d of 380 mm.

Acknowledgements

The work was supported by the Henan key research and development program (241111320900), the key technologies R&D program of Henan province (252102320163) and the guiding fund of government's science and technology (Z20241471018), R&D Project of Anyang Cigarette Factory, China Tobacco Henan Industrial Co., Ltd. (BWQ202503).

References

[1] Takale B B, Patil R S. Studies on drying characteristics of Thompson seedless grapes using mixed mode forced convection solar dryer[J]. Energy, 2025, 326: 136298.

[2] Laleman F, Mathot F, Bourlès E, et al. The influence of thermal radiation during microwave-assisted freeze-drying of pharmaceutical unit doses[J]. International Journal of Pharmaceutics, 2024, 664: 124640.

[3] Gao L, Fix A, Seabourne T, et al. A comprehensive review of heat pump wood drying technologies[J]. Energy, 2024, 311: 133241.

[4] Gao X, Xuan C, Tang Z, et al. A dynamic drying process: Mathematical modeling and energy consumption optimization of alfalfa bales using hot air drying[J]. Renewable Energy, 2025, 246: 122961.

[5] Chen P, Xiong Z, Xu J, et al. Simulation and parameter optimization of high moisture rice drying on combine harvester before threshing[J]. Computers and Electronics in Agriculture, 2023, 215: 108451.

[6] Kumar B, Patle S D, Dewangan S K. Solar drying of ginger (Zingiber officinale) and turmeric (Curcuma longa): A comprehensive review[J]. Solar Energy, 2025, 299: 113748.

[7] Guan X, Wang Y, Li M, et al. Research on the performance of heat pump drying system with

698 rock thermal energy storage[J]. Energy, 2025, 316: 134510.

699 [8] Chen X, Wang D, Wang Y, et al. CFD design and testing of an air flow distribution device for
700 microwave infrared hot-air rolling-bed dryer[J]. Biosystems Engineering, 2024, 246: 204-218.

701 [9] Amjad W, Chen Z, Ambrose K. Design assessment of grain inverters in cross-flow grain dryer
702 via CFD-DEM numerical simulation[J]. Biosystems Engineering, 2024, 239: 147-157.

703 [10] Li G, Zhang H, Ye X, et al. Determination of optimal air supply form on sludge convective
704 drying process: A CFD-DEM study[J]. Powder Technology, 2024, 444: 120052.

705 [11] Ross C, Sablani S, Tang J. Preserving Ready-to-Eat Meals Using Microwave Technologies for
706 Future Space Programs[J]. Foods, 2023, 12(6).

707 [12] Lan B, Zhao P, Xu J, et al. CFD-DEM-IBM simulation of particle drying processes in gas-
708 fluidized beds[J]. Chemical Engineering Science, 2022, 255: 117653.

709 [13] Gai Y, Zhang Z, Wang X. The influence of various layouts of internal baffles on air distribution
710 in heat pump cabinet dryers[J]. International Communications in Heat and Mass Transfer, 2024, 159:
711 108209.

712 [14] Ahmadi Babadi K, Khorasanizadeh H, Aghaei A. CFD modeling of air flow, humidity, CO2
713 and NH3 distributions in a caged laying hen house with tunnel ventilation system[J]. Computers and
714 Electronics in Agriculture, 2022, 193: 106677.

715 [15] Lv H, Su D, Lv W, et al. Design of microwave hot-airflow vibrating drying equipment for initial
716 drying and enzymatic inactivation of fresh fruits and vegetables[J]. Drying Technology, 2022, 40(8):
717 1688-1702.

718 [16] Cao M, Yang R, Choi C Y, et al. Effects of discharge angle of jet from a slot orifice on cooling
719 performance for a perforated air ducting system in dairy cattle barn[J]. Computers and Electronics in
720 Agriculture, 2023, 210: 107890.

[17] Wang D, Tan L, Yuan Y, et al. Design of integrated air impingement blanching and drying equipment for grape and airflow uniformity analysis and optimization of its drying material room[J]. Journal of Mechanical Science and Technology, 2024, 38(4): 2123-2142.

[18] Mondal S, Dutta S, Pande P, et al. Intensify staple fibre drying by optimizing air distribution in multistage convective dryer using CFD[J]. Chemical Engineering and Processing - Process Intensification, 2022, 173: 108807.

[19] Liu Z, Sun B, Cui H, et al. Improvement of airflow uniformity and noise reduction with optimized V-shape configuration of perforated plate in the air distributor[J]. Indoor and Built Environment, 2024, 33(4): 641-657.

[20] Ibrahim M, Harkouss F, Biwole P, et al. Multi-objective hyperparameter optimization of artificial neural network in emulating building energy simulation[J]. Energy and Buildings, 2025, 337: 115643.

[21] Miranda M H R, Silva F L, Frutuoso F S, et al. Novel prediction approach for exhaust gases using Elman neural network combined with particle swarm optimization[J]. Energy, 2025, 331: 136769.

[22] Yibo W, Huaishuang S, Jingjie W, et al. Study on artificial neural network prediction of heat transfer in vertically upward internally rifled tubes with supercritical water[J]. Annals of Nuclear Energy, 2025, 220: 111539.

[23] Zheng L, Wang Z, An T, et al. Investigating the influence of Cr-Ti synergy on microstructure and low-temperature toughness in X80 pipeline steel deposited metal using BP artificial neural network[J]. Materials Today Communications, 2025, 47: 113103.

[24] Le T M, Atroshchenko E, Bui T Q, et al. Material and thickness optimization of microscale in-plane FG thin-walled structures using deep neural network-assisted artificial hummingbird

744 algorithms[J]. Composite Structures, 2025, 368: 119227.

745 [25] Zhao Y, Xuan S, Wang Y, et al. Reliability-based multi-objective optimization design of
746 composite patch repair structure using artificial neural networks[J]. Composite Structures, 2025, 352:
747 118692.

748 [26] Jin Q, Chen X, Yang C, et al. Optimization of heat exchanger with biomimetic shark skin riblet
749 structure using artificial neural network[J]. International Journal of Heat and Fluid Flow, 2025, 112:
750 109720.

751 [27] Wu MY, Yuan XY, Chen ZH, et al. Airfoil shape optimization using genetic algorithm coupled
752 deep neural networks[J]. Physics of Fluids, 2023, 35(8): 085140.

753 [28] Deb K, Pratap A, Agarwal S, et al. A fast and elitist multiobjective genetic algorithm: NSGA-
754 II[J]. IEEE Transactions on Evolutionary Computation, 2002, 6(2): 182-197.

755 [29] Chen G, Sun M, Li J, et al. Study on high-altitude ceiling strategy of compression ignition
756 aviation piston engines based on BP-NSGA II algorithm optimization[J]. Energy, 2024, 294: 130966.

757 [30] Ye L, Li C, Wang C, et al. A multi-objective optimization approach for battery thermal
758 management system based on the combination of BP neural network prediction and NSGA-II
759 algorithm[J]. Journal of Energy Storage, 2024, 99: 113212.

760 [31] Zhang J, Zhang L, Ren P, et al. Multi-objective optimization prediction model for building
761 parameters of photovoltaic windows based on NSGA II-BP[J]. Case Studies in Thermal Engineering,
762 2024, 64: 105500.

763 [32] Liu Y, Li M, Li Q, et al. Parameter optimization of L-joint of composite sandwich structure
764 based on BP-GA algorithm[J]. Composite Structures, 2022, 289: 115508.

765 [33] Yao J, Zhang Z, Saari J, et al. Structure optimization of intercooler bionic fins based on artificial
766 neural network and genetic algorithms[J]. Energy, 2024, 307: 132615.

[34] Jin L, Xi H. Multi-objective parameter optimization of the Z-type air-cooling system based on artificial neural network[J]. Journal of Energy Storage, 2024, 86: 111284.

[35] Fu H, Luan J, Yang L, et al. Multi-objective optimization of jet impingement cooling structure with smooth target surface and enhanced target surface in a limited space[J]. International Communications in Heat and Mass Transfer, 2024, 159: 108192.

[36] Wang Z, Kong F, Chan W, et al. Study on the effect of wind direction on the thermal performance of cavity receiver for trough solar system: Artificial neural network approach based on genetic algorithm[J]. Energy, 2025, 320: 135287.